NANO: Brief Reports and Reviews
Vol. 15, No. 9 (2020) 2050117 (12 pages)

DOI: 10.1142/S1793292020501179

World Scientific
www.worldscientific.com

Graphene-Wrapped $ZnMn_2O_4$ Nanoparticles with Enhanced Performance as Lithium-Ion Battery Anode Materials

Meng Sun*, Sijie Li*, Jiajia Zou*, Zhipeng Cui*, Qingye Zhang*, François Schiettekatte†, David Barba‡, Bing Liu*,§,‖ and Yiqian Wang*,¶,‖

*College of Physics, Qingdao University
No. 308 Ningxia Road
Qingdao 266071, P. R. China

†Département de Physique et Regroupement
Québécois sur les Matériaux
de Pointe Université de Montréal, Case Postale 6128
Succursale Centre-Ville
Montréal, Québec H3C 3J7 Canada

‡INRS-Énergie, Matériaux et Télécommunications
1650 boulevard Lionel-Boulet
Varennes, Québec J3X1S2, Canada
§bing_liu@qdu.edu.cn
¶yqwang@qdu.edu.cn

Received 29 February 2020
Accepted 8 July 2020
Published 10 September 2020

$ZnMn_2O_4$ nanoparticles (NPs) wrapped by reduced graphene oxide (rGO) were fabricated *via* a two-step solvothermal method and used as an anode material for lithium-ion batteries (LIBs). Compared to pure $ZnMn_2O_4$, the $ZnMn_2O_4$ NPs/rGO composites deliver higher capacities of 1230 mAh g^{-1} and 578 mAh g^{-1} after 200 cycles at a current density of 100 mA g^{-1} and 500 mA g^{-1}, respectively. The enhanced electrochemical performance of $ZnMn_2O_4$ NPs/rGO composites is mainly attributed to a distinctive structure ($ZnMn_2O_4$ NPs surrounded by flexible rGO), which can promote the diffusion of Li^+, accelerate the transport of electrons and buffer volume expansion during the Li^+ insertion/extraction process. Furthermore, the rGO sheets can effectively prevent the agglomeration of $ZnMn_2O_4$ NPs, thus, improving structural stability of the composites. The excellent electrochemical performance indicates that such $ZnMn_2O_4$ NPs/rGO composite structure has a great potential for high-performance LIBs.

Keywords: LIBs; $ZnMn_2O_4$ NPs; rGO; electrochemical performance.

‖Corresponding authors.

1. Introduction

The emergence of numerous high-tech products, such as electronic portable devices, electric vehicles and unmanned aerial vehicles, results in a great demand for storage devices with high energy density. Lithium-ion batteries (LIBs) are currently the dominant type of energy storage in most applications, and there is a lot of market pressure to improve their cycling stability and rate capability.[1–5] Especially, the performance of anode materials plays a decisive role for LIBs. Therefore, it is necessary to develop the anode materials with high specific capacity, good rate capability and long cycle life. Over the past two decades, transition metal oxides have been considered as potential candidates to replace traditional graphite anode materials due to their high capacity, environmental friendliness and low cost.[6,7] Compared with single transition metal oxides, mixed transition metal oxides possess advantages of diversity and complementarity, and exhibit better performance in the application of anode materials.[8–11] Recently, metal-oxide nanomaterials with a spinel structure (AB_2O_4) have been widely explored due to their superior electrochemical properties. Among them, $ZnMn_2O_4$ has shown great advantages due to its low cost, environmental friendliness and relatively low operating voltage.[12–15] However, $ZnMn_2O_4$ electrodes suffer from serious pulverization problems caused by large volume change, leading to a rapid capacity fading. Meanwhile, low electrical and ionic migration can lead to inferior rate capability.[16–18] To overcome these drawbacks, one strategy is to design different morphologies and microstructures to obtain strong structural stability; the other is to design composite materials such as carbon coating.[19,20] Recent studies have demonstrated that the electrochemical performance of transition metal oxides can be significantly improved by compounding with graphene.[14,15]

Since the discovery of graphene in 2004, it has attracted great research interest due to its unique electronic properties, high electrical conductivity and large specific surface area.[21–23] Benefiting from these excellent properties, graphene has been considered as an ideal conductive material for LIBs.[24] In recent years, composites of metal oxides and graphene have exhibited great improvement in electrochemical applications, such as high reversible capacity, long cycle life and good rate performance.[25,26] Therefore, the synthesis of a hybrid of $ZnMn_2O_4$ and graphene should be a good strategy for high-performance LIBs.

In this work, $ZnMn_2O_4$ NPs wrapped by reduced graphene oxide (rGO) were prepared using a two-step solvothermal method. When used as anode materials for LIBs, the $ZnMn_2O_4$ NPs/rGO composites exhibit higher reversible capacity and better rate performance than pure $ZnMn_2O_4$ NPs. This is attributed to the unique structure of $ZnMn_2O_4$ NPs/rGO composites, which can accelerate electron transfer, facilitate the diffusion of Li^+ and buffer large volume change during the Li^+ insertion/extraction process.

2. Experimental

2.1. *Chemical reagents*

Ethylene glycol (EG, $(CH_2OH)_2$, 99.0%), zinc acetylacetonate ($Zn(acac)_2$, $C_{10}H_{14}ZnO_4$, 99.0%), manganese acetylacetonate ($Mn(acac)_2$, $C_{10}H_{14}MnO_4$, 98.5%) and cetyltrimethylammonium bromide (CTAB, $C_{16}H_{33}(CH_3)_3NBr$, 99.0%) were purchased from Sinopharm Chemical Reagent Co., Ltd. All chemicals were of analytical grade and were used as received without further purification.

2.2. *Synthesis of $ZnMn_2O_4$ NPs*

$ZnMn_2O_4$ NPs were synthesized by a facile solvothermal method.[27] 2.0 g CTAB was dissolved in 50 mL EG to form a homogeneous solution under vigorous stirring at room temperature. Afterwards, $Zn(acac)_2$ and $Mn(acac)_2$ (a molar ratio of 1:1) were added into the above solution and then subjected to ultrasonic treatment for 30 min. Subsequently, the mixed solution was stirred for 15 min, and then transferred into a 100 mL Teflon-sealed autoclave and maintained at 180°C for 13 h to obtain the precursor. After the autoclave was cooled to room temperature, the resulting precipitates were collected by centrifugation, washed several times with distilled water and ethanol, and then dried at 60°C for 6 h. Finally, the resulting precursor was calcined at 600°C in air for 3 h at a heating rate of 4°C/min.

2.3. *Synthesis of $ZnMn_2O_4$ NPs/rGO composites*

Graphene oxide (GO) was synthesized using natural graphite by a modified Hummers' method.[28]

0.03 g of GO was dispersed in a mixed solution of 30 mL EG and 15 mL distilled water, stirred continuously to form a homogeneous solution. Afterwards, 0.20 g $ZnMn_2O_4$ NPs were added into the above solution under strong stirring until they were completely dissolved. Subsequently, the mixture solution was transferred into a 100 mL Teflon-sealed autoclave and maintained at 150°C for 2 h. The final precipitates were collected by centrifugation, and dried at 60°C overnight. Finally, the resulting mixture was annealed at 400°C under an argon atmosphere for 2 h with a heating rate of 4°C/min to obtain $ZnMn_2O_4$ NPs/rGO composites.

2.4. *Material characterization*

X-ray diffraction (XRD) analysis was carried out on a SmartLab XRD diffractometer with Cu-Kα_1 radiation ($\lambda = 1.5406$ Å). Thermogravimetric analysis (TGA) was conducted on a Netzsch TG 209 apparatus under an air flow from room temperature to 900°C at a heating rate of 10°C/min. Raman spectra were recorded on an RM 2000 microscopic confocal Raman spectrometer (Renishaw PLC, England) using a 514-nm laser line for the excitation. X-ray photoelectron spectroscopy (XPS) was performed on a Thermo Scientific ESCALAB 250Xi instrument with monochromatic Al Kα radiation ($h\nu = 1486.6$ eV) at ultrahigh vacuum (below 10–8 Pa). The morphology of the samples was characterized by scanning electron microscopy (SEM, Hitachi S-4800). Bright-field (BF) images and high-resolution transmission electron microscopy (HRTEM) images were obtained on a JEOL JEM2100F transmission electron microscope (TEM) with an accelerating voltage of 200 kV. Nitrogen adsorption–desorption tests were carried out on an automatic volumetric sorption analyzer (NOVA 1100, Quantachrome, USA) at 77 K. The Brunauer–Emmett–Teller (BET) method was used to calculate the specific surface areas of the $ZnMn_2O_4$ NPs/rGO composites. The Barrett–Joyner–Halenda (BJH) method was used to determine the pore size from the desorption branches of the isotherms.

2.5. *Electrochemical measurements*

The working electrodes were prepared by mixing the active materials ($ZnMn_2O_4$ NPs, and $ZnMn_2O_4$ NPs/rGO composites) with carbon black and water-soluble sodium alginate (SA) in a weight ratio of 70:15:15 (wt.%) onto a pure copper foil. The electrodes were dried in a vacuum oven at 120°C for 12 h and the cells were assembled in a glove box full of argon with a moisture and oxygen concentration of less than 1 ppm. The mass loading of the active materials for the cell testing was 1.5 mg cm^{-2}. To evaluate the relevant electrochemical properties, CR2025-type coin cell batteries were assembled with a lithium metal as a counter electrode. The electrolyte consisted of 1 M $LiPF_6$ solution of ethylene carbonate (EC)/dimethyl carbonate (DMC)/diethyl carbonate (DEC) (1:1:1 in volume). The electrochemical performance was tested on a LAND CT2001 battery test system in a voltage range from 0.01 V to 3.00 V at room temperature. Cyclic voltammetry (CV) measurements (over the potential range from 0.01 V to 3.00 V at a scan rate of 0.1 mV s^{-1}) and electrochemical impedance spectroscopy (EIS) tests were performed on a Metrohm Autolab electrochemical workstation (PGSTAT 302N) at a frequency range from 100 kHz to 0.01 Hz with a disturbance amplitude of 5 mV.

3. Results and Discussion

Figure 1 shows the XRD patterns of $ZnMn_2O_4$ NPs and $ZnMn_2O_4$ NPs/rGO composites. Both patterns exhibit diffraction peaks at 18.23°, 29.32°, 31.25°, 33.00°, 36.41° and 60.83°, which can be well indexed to the (101), (112), (020), (103), (211) and (224) planes of the tetragonal $ZnMn_2O_4$ phase (JCPDS no.: 77-0470, $a = b = 5,720$ Å, $c = 9.240$ Å). The sharp diffraction peaks indicate that the $ZnMn_2O_4$ and $ZnMn_2O_4$ NPs/rGO samples have good crystallinity. In the XRD pattern of

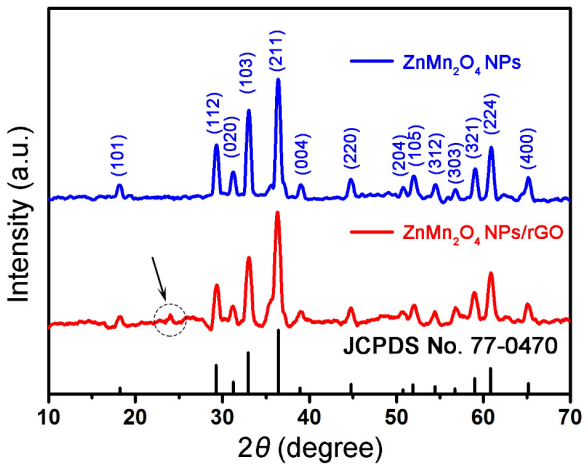

Fig. 1. XRD patterns of $ZnMn_2O_4$ NPs and $ZnMn_2O_4$ NPs/rGO composites.

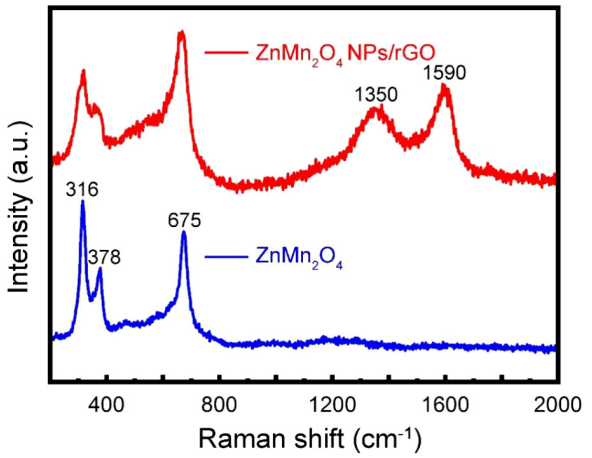

Fig. 2. Raman spectra of $ZnMn_2O_4$ NPs and $ZnMn_2O_4$ NPs/rGO composites.

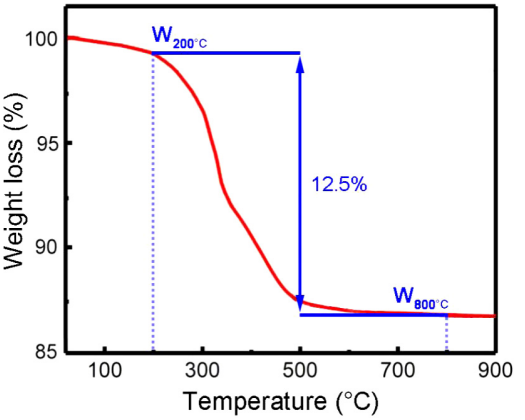

Fig. 3. TGA curve of $ZnMn_2O_4$ NPs/rGO composites.

$ZnMn_2O_4$ NPs/rGO composites, a weak peak observed around 24° could be ascribed to the (002) reflections of the graphene sheets.[29] No obvious GO peaks can be found, which is ascribed to its low mass content.

To further confirm the existence of graphene in the composite, Raman investigations of $ZnMn_2O_4$ NPs and $ZnMn_2O_4$ NPs/rGO composites were conducted, as shown in Fig. 2. It is observed that both $ZnMn_2O_4$ NPs/rGO composites and $ZnMn_2O_4$ NPs exhibit three Raman peaks at 316 cm^{-1}, 378 cm^{-1} and 675 cm^{-1}, in good agreement with the characteristic Raman vibration modes of $ZnMn_2O_4$ reported in the previous literature.[30] Moreover, for the $ZnMn_2O_4$ NPs/rGO composites, two characteristic peaks observed around 1350 cm^{-1} and 1590 cm^{-1} are ascribed to the disordered (D) and graphitic (G) bands of graphene, respectively.[31,32] The D-band originates from the disordered carbon, whereas the G-band derives from graphitic carbon.[31,32] Therefore, it is concluded that graphene is present in the composites.

To determine the mass proportion of rGO in $ZnMn_2O_4$ NPs/rGO composites, a TGA test was carried out in a temperature range from 30°C to 900°C. Figure 3 shows the TGA curve of the composites, from which it can be seen that the composites exhibit a small weight loss below 200°C and an apparent weight loss between 200°C to 800°C. The small weight loss below 200°C is caused by the vaporization of adsorbed water, while the weight loss between 200°C to 800°C results from the oxidation of rGO in air.[33,34] No weight loss is observed between 800°C and 900°C, indicating that the structure of $ZnMn_2O_4$ remains stable above 800°C. Therefore, the mass proportion of rGO in the composites can be calculated to be about 12.5%, as shown in Fig. 3, which is very close to the weight percentage (13%) of GO added into the composite.

XPS analyses were used to investigate the surface chemical compositions and the elemental valance states of the $ZnMn_2O_4$ NPs/rGO composites. The survey spectrum in Fig. 4(a) demonstrates that the composites consist of Zn, Mn, O and C elements. The Zn 2*p* spectrum in Fig. 4(b) exhibits two peaks at binding energies of 1044.6 eV and 1021.2 eV, which correspond to Zn $2p_{1/2}$ and $2p_{3/2}$, respectively. This indicates the presence of stable Zn^{2+} in the composite.[35] The peaks at binding energies of 653.8 eV and 641.8 eV in the Mn 2*p* spectrum in Fig. 4(c) can be assigned to Mn $2p_{1/2}$ and $2p_{3/2}$, respectively. It is worth mentioning that the energy difference between Mn 2*p*1/2 and Mn $2p_{3/2}$ is approximately 11.9 eV, which is in good agreement with that of $ZnMn_2O_4$.[36–38] This characteristic implies that the oxidation state of Mn in $ZnMn_2O_4$ NPs/rGO is Mn^{3+} rather than Mn^{2+} or Mn^{4+}.[36–38] The asymmetric O 1s spectrum can be divided into two peaks, as shown in Fig. 4(d). One stronger peak at 529.8 eV indicates the characteristics of lattice oxygen in the metal (Mn, Zn) oxide. The other peak at 531.5 eV implies the contribution of the remaining unreduced GO and adsorbed oxygen, such as −OH and H_2O on the surface.[37,39] As observed in Fig. 4(e), the C 1*s* spectrum of the $ZnMn_2O_4$ NPs/rGO composites consists of four different peaks with binding energies of 284.6 eV, 286.3 eV, 287.1 eV and 288.1 eV, which can be ascribed to graphitic C=C/C–C, C–O, C=O and COOH bonds, respectively.[40]

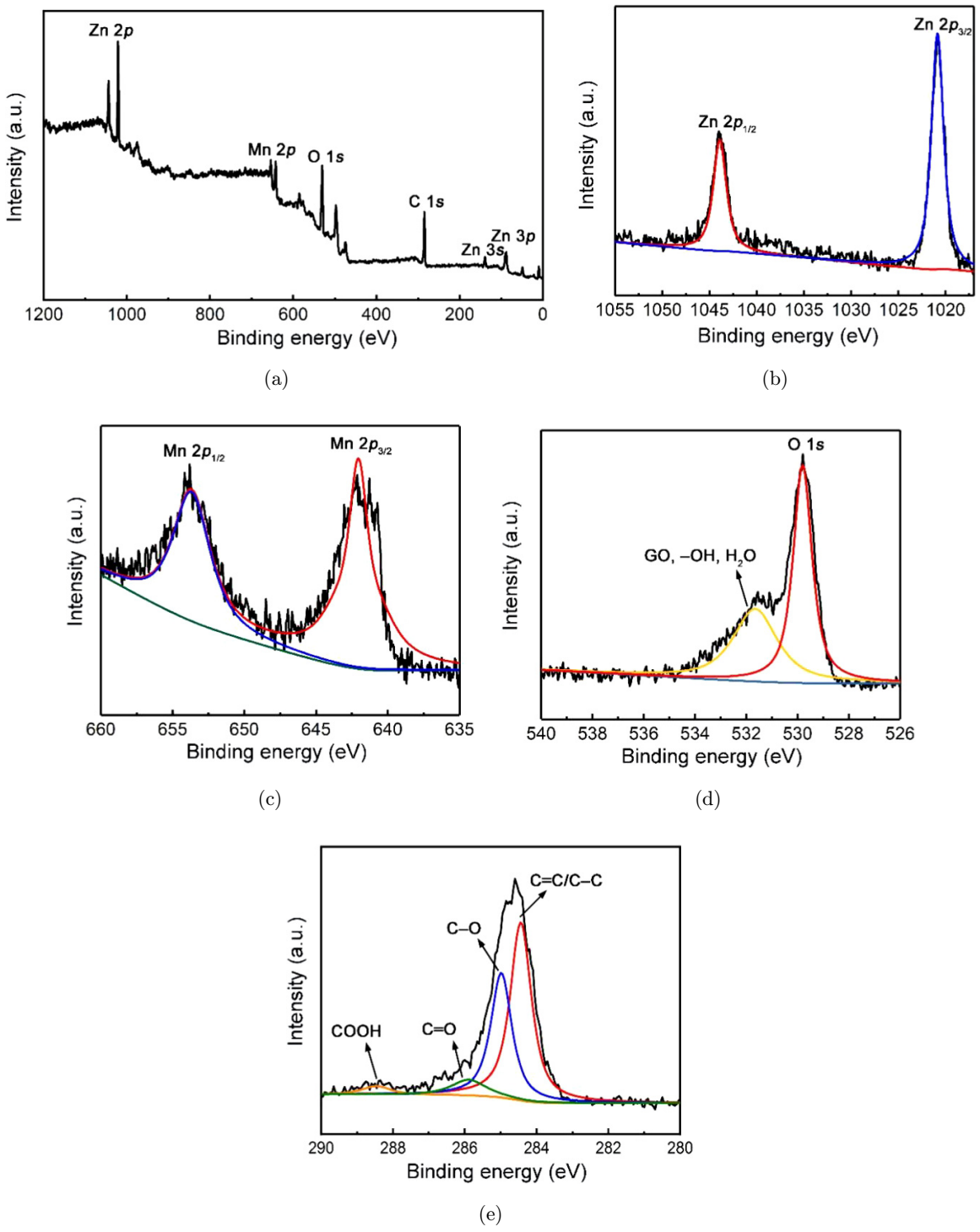

Fig. 4. XPS spectrum of the $ZnMn_2O_4$ NPs/rGO composites: (a) survey spectrum, (b) Zn 2*p*, (c) Mn 2*p*, (d) O 1*s* and (e) C 1*s*.

These results indicate that the valence states of the elements in the composites are Zn^{2+}, Mn^{3+} and O^{2-}, respectively.

The morphologies of $ZnMn_2O_4$ NPs and $ZnMn_2O_4$ NPs/rGO composites were investigated by SEM. Figures 5(a) and 5(b) show the SEM images of $ZnMn_2O_4$ NPs, from which it can be seen that the NPs have a diameter ranging from 10 nm to 25 nm. Figures 5(c) and 5(d) present the low-magnification and high-magnification SEM images

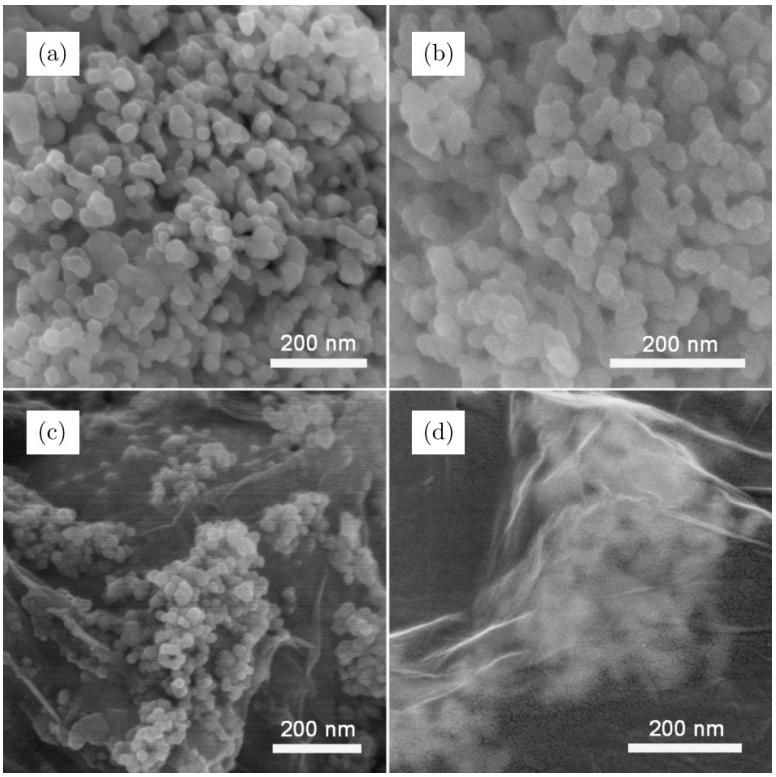

Fig. 5. Low-magnification (a) and high-magnification (b) SEM images of $ZnMn_2O_4$ NPs. Low-magnification (c) and high-magnification (d) SEM images of $ZnMn_2O_4$ NPs/rGO composites.

of $ZnMn_2O_4$ NPs/rGO composites. It can be seen from the image that $ZnMn_2O_4$ NPs are wrapped by membrane-like rGO, forming a hierarchical pizza-like structure of $ZnMn_2O_4$ NPs/rGO composites. The introduction of graphene is beneficial to the formation of continuous conductive network. In addition, the rGO sheets can efficiently prevent agglomeration of particles. Such a composite structure can facilitate the transmission of electrons in the materials, thus leading to the high electronic conductivity.

TEM examinations were carried out to investigate the microstructure of $ZnMn_2O_4$ NPs and $ZnMn_2O_4$ NPs/rGO composites in details. Figure 6(a) shows a typical BF image of $ZnMn_2O_4$ NPs. The as-prepared $ZnMn_2O_4$ NPs observed from the image are uniform, with an average diameter of 18 nm. Figure 6(b) presents a single $ZnMn_2O_4$ NP with a diameter of about 16 nm, which is almost spherical. The lattice spacings are measured to be 4.86 Å and 2.86 Å, which are consistent with the (101) and (020) planes of the tetragonal $ZnMn_2O_4$, respectively. Figure 6(c) presents a typical BF TEM image of $ZnMn_2O_4$ NPs/rGO composites. It is observed that numerous $ZnMn_2O_4$ NPs distribute on the surface of rGO sheet. Figure 6(d) shows a typical HRTEM image of the region enclosed by a red square in Fig. 6(c). The lattice spacings measured from the image are 2.86 Å and 2.47 Å, corresponding to the (020) and (211) planes of the tetragonal $ZnMn_2O_4$ phase, respectively. This wrapping design contributes to the formation of continuous conductive networks that promote rapid transport of electrons.

Figure 7 shows the nitrogen adsorption–desorption isotherms and corresponding pore size distribution curves of the $ZnMn_2O_4$ NPs/rGO composite. As shown in Fig. 7(a), the samples show physisorption isotherms of type IV with a hysteresis loop of type H_3 in the range 0.5–1.0 P/P_0, which is one of the characteristics for the mesopores. Figure 7(b) presents the corresponding pore size distribution calculated by the BJH method from the desorption branch, demonstrating a narrow pore size distribution of 15–22 nm centered at around 19.7 nm. This further confirms that the pores in the composite possess characteristic of mesopores.[41] Correspondingly, the BET surface area and the pore volume of the composite are calculated to be 123.16 $m^2 g^{-1}$ and 0.354 $cm^3 g^{-1}$. This mesoporous structure with a large specific surface area not only promotes the

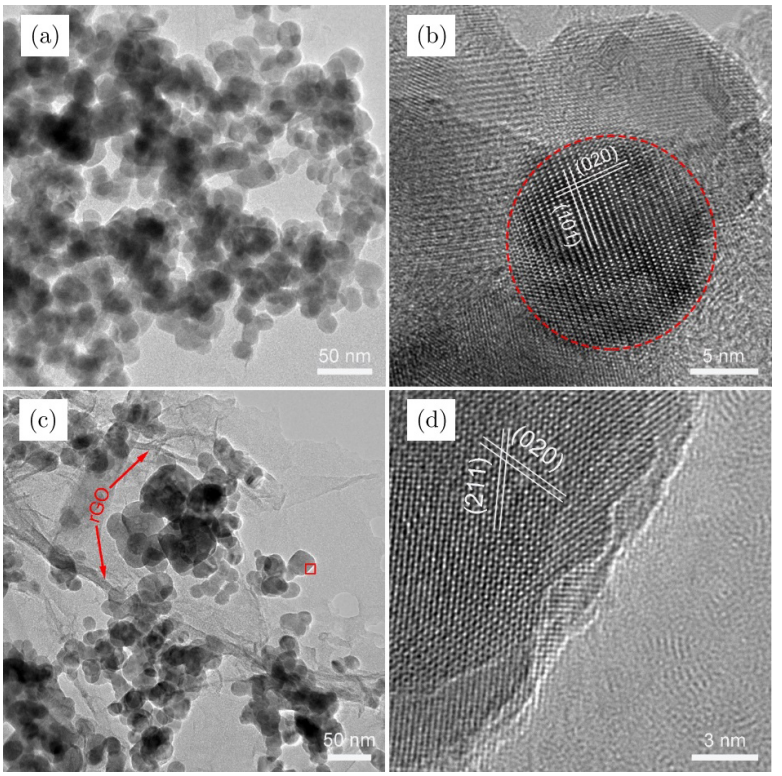

Fig. 6. Typical BF TEM image (a) and HRTEM image (b) of $ZnMn_2O_4$ NPs. Red circle indicates a single $ZnMn_2O_4$ NP. (c) Typical BF TEM image of $ZnMn_2O_4$ NPs/rGO composites. (d) Enlarged HRTEM image of the region enclosed by a red square in (c) (color online).

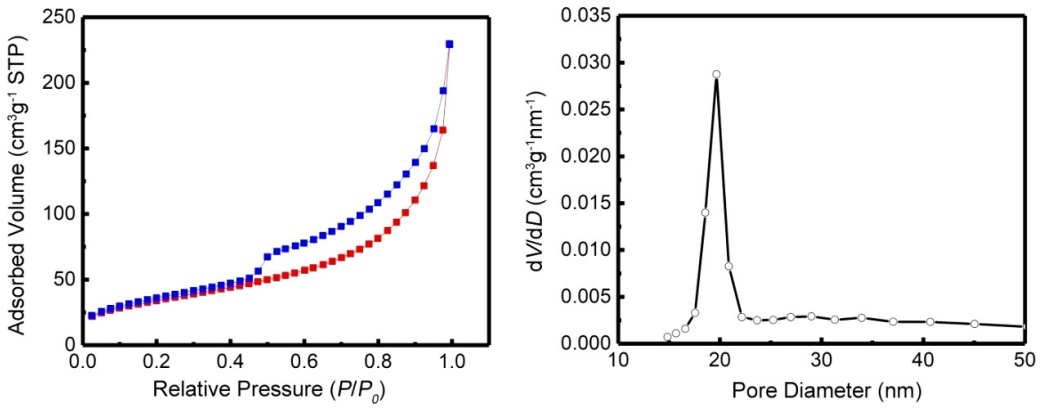

(a) (b)

Fig. 7. (a) Nitrogen adsorption–desorption isotherms and (b) the corresponding pore size distribution curves of $ZnMn_2O_4$ NPs/rGO composite.

diffusion of Li^+ in the electrode and keeps the effective contact between electrode and electrolyte, but also provides more active sites for the reaction of Li^+.[31,42,43] Therefore, we infer that the $ZnMn_2O_4$ NPs/rGO composite can provide a good platform for the storage of Li^+.

The electrochemical properties of the $ZnMn_2O_4$ NPs/rGO composites are investigated by CV and galvanostatic charge–discharge measurements. Figure 8(a) illustrates the first six CV curves within a voltage range between 0.01 V and 3.0 V using a scan rate of 0.1 mV s^{-1}. In the first cathodic scan, two obvious reduction peaks can be observed at 0.87 V and 0.14 V. The broad peak at 0.87 V, which vanishes in the subsequent scans, can be ascribed to the irreversible reduction of Mn^{3+} to Mn^{2+}.[44]

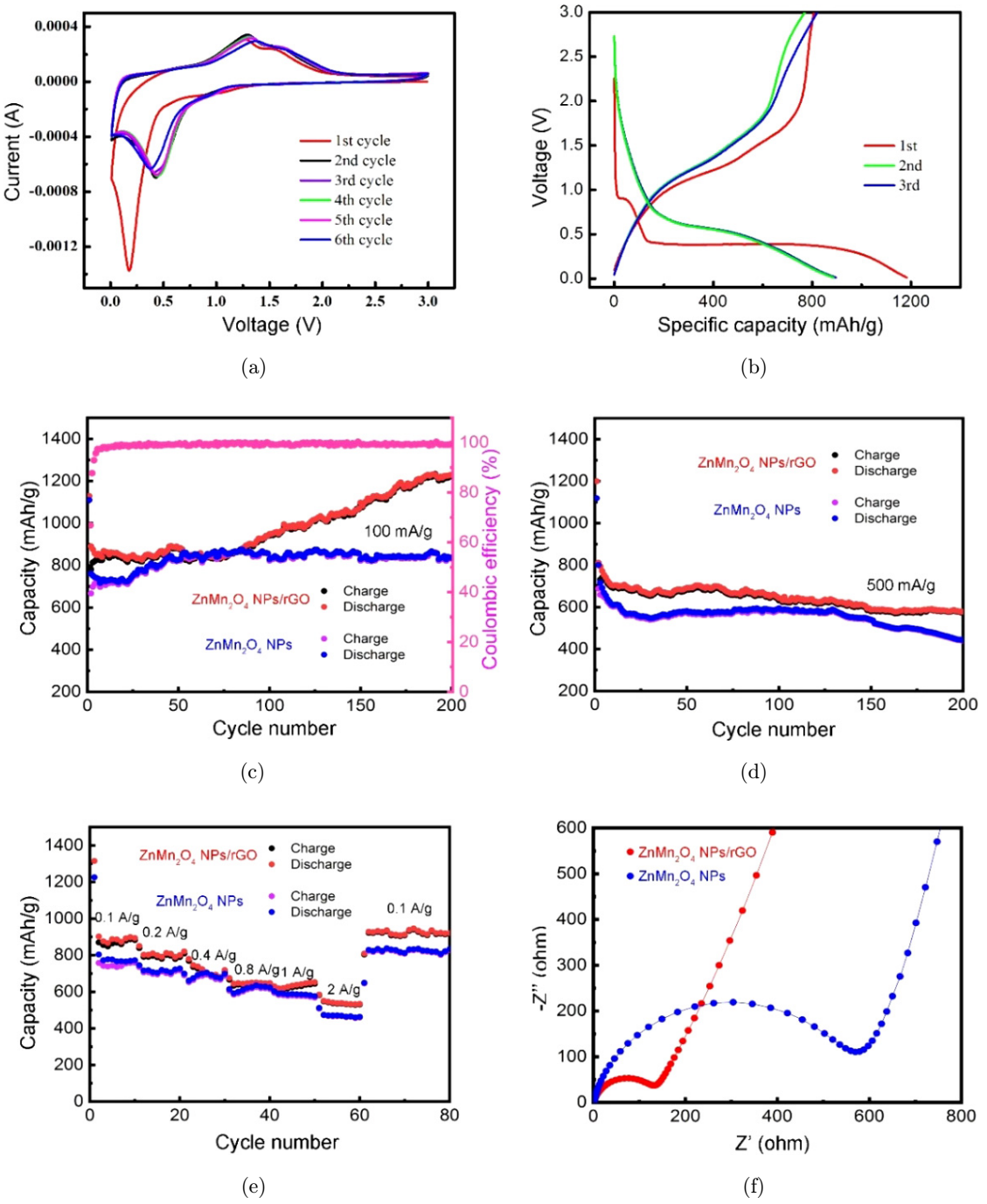

Fig. 8. (a) CV curves at 0.1 mV s^{-1} and (b) initial voltage versus capacity curves at 100 mA g^{-1} of $ZnMn_2O_4$ NPs/rGO composite electrode. Cycling performance of $ZnMn_2O_4$ NPs and $ZnMn_2O_4$ NPs/rGO electrodes at a current density of 100 mA g^{-1} (c) and 500 mA g^{-1} (d). (e) Rate performance at various current densities and (f) EIS plots of $ZnMn_2O_4$ NPs and $ZnMn_2O_4$ NPs/rGO composite electrodes.

The sharp peak around 0.14 V is associated with the following three processes: (i) the formation of a solid electrolyte interphase (SEI) caused by the decomposition of electrolyte, (ii) the reduction of Mn^{2+} and Zn^{2+} to Mn^0 and Zn^0 in Li_2O matrix and (iii) the alloying process of Zn with Li to form ZnLi.[31] In the first anode scan, two broad oxidation peaks are observed at 1.2 V and 1.5 V, which are related to the oxidation processes of Mn^0 to Mn^{2+} and Zn^0 to Zn^{2+}, respectively, along with the decomposition of Li_2O matrix.[45] In the second cycle, the cathodic peak is shifted to 0.45 V, while almost no change is

found in the anodic process. From the second cycle, the CV curves are almost the same, which indicates the high reversibility of the $ZnMn_2O_4$ NPs/rGO composites during the charge/discharge process. The electrochemical reactions of $ZnMn_2O_4$ NPs/rGO composites during the charge/discharge process can be described by the following equations[11,43,46,47]:

$$ZnMn_2O_4 + 9Li^+ + 9e^- \rightarrow 2Mn + ZnLi + 4Li_2O, \quad (1)$$

$$2Mn + ZnLi + 3Li_2O \leftrightarrow 2MnO + ZnO + 7Li^+ + 7e^-. \quad (2)$$

Figure 8(b) shows the first three cycles galvanostatic charge–discharge curves of the $ZnMn_2O_4$ NPs/rGO composite electrode cycled at a current density of 100 mA g^{-1} for voltages varying between 0.1 V and 3 V. In the first discharge process, two obvious voltage platforms are observed at 0.87 V and 0.45 V, corresponding to the reduction of Mn^{3+} to Mn^{2+} and the formation of Mn^0, Zn^0 and ZnLi, in agreement with the CV results of Fig. 8(a). The first discharge capacity is 1129 mAh g^{-1} and the first charge capacity is 754 mAh g^{-1} with an initial Coulombic efficiency of 66.8%. The irreversible loss of 375 mAh g^{-1} results from the formation of SEI layer around the electrode, which is very common in most anode materials.[48] Compared to the first discharge curve, the second discharge curve exhibits a lower capacity with a higher voltage platform. The third charge/discharge curve almost coincides with the second one, indicating that $ZnMn_2O_4$ NPs/rGO composite electrode possesses good cycling stability.

Figures 8(c) and 8(d) illustrate the cycling performance of $ZnMn_2O_4$ NPs and $ZnMn_2O_4$ NPs/rGO electrodes at a current density of 100 mA g^{-1} and 500 mA g^{-1}, respectively. As shown in Fig. 8(c), $ZnMn_2O_4$ NPs/rGO electrode delivers a first discharge capacity of 1129 mAh g^{-1}, and reaches 1230 mAh g^{-1} after 200 cycles at a current density of 100 mA g^{-1}. Even at a high current density of 500 mA g^{-1}, the discharge capacity of $ZnMn_2O_4$ NPs/rGO electrode maintains a value of 578 mAh g^{-1} after 200 cycles in Fig. 8(d). It is worth noting that the discharge capacity of $ZnMn_2O_4$ NPs/rGO slightly decreased in the first 75 cycles, and then increases significantly in the subsequent cycles in Fig. 8(c). Because of the formation of an organic polymer gel-like layer which originates from the incomplete decomposition of the electrolyte, the specific capacity decreased in the initial several cycles. Then the specific capacity increased significantly, which can be ascribed to the following points: (i) With the increasing cycles, the electrode material is gradually pulverized, providing more active sites for Li^+ storage. In the meantime, the pulverized particles are still attached onto the surface of the rGO sheets, leading to the increase of capacity. (ii) The rGO sheets increase the conductivity of the electrodes. Hence, the charge transfer rate can be increased, thus improving the capacity. (iii) A so-called "pseudocapacitance-type" effect caused by the formed polymeric gel-like film on the surface of electrode materials has a significant contribution to the enhanced capacity.[31,49,50] Without the rGO support, however, the discharge capacity of $ZnMn_2O_4$ NPs barely increased, due to their poor electronic conductivity and severe aggregation upon the cycling.

Figure 8(e) shows the rate capability of pure $ZnMn_2O_4$ and $ZnMn_2O_4$ NPs/rGO composite electrodes. The average capacities of $ZnMn_2O_4$ NPs/rGO electrode are calculated to be 943, 851, 810, 785, 719, 630 and 920 mAh g^{-1} at current densities of 0.1, 0.2, 0.4, 0.8, 1.0, 2.0 and 0.1 A g^{-1}, which are much better than those of $ZnMn_2O_4$ electrode. The discharge capacity of $ZnMn_2O_4$ NPs/rGO electrode is found to decrease with the increase of current density, because large currents can induce the polarization effects and reduce the diffusion process.[51,52] Moreover, when the current density drops back to 0.1 A g^{-1}, the reversible capacity of $ZnMn_2O_4$ NPs/rGO electrode is restored to 920 mAh g^{-1}. For the $ZnMn_2O_4$ NPs electrode, when the current density returns to 0.1 A g^{-1}, the reversible capacity is about 810 mAh g^{-1}. This proves that the $ZnMn_2O_4$ NPs/rGO electrode exhibits enhanced rate capability compared to the $ZnMn_2O_4$ NPs electrode during the discharge/charge process.

The electrochemical performances of $ZnMn_2O_4$ nanostructures in the previous literature are summarized in Table 1. From this table, it can be seen that the $ZnMn_2O_4$ NPs/rGO composite in our work exhibits superior electrochemical performances compared to previously-reported $ZnMn_2O_4$ nanostructures. Thus, the $ZnMn_2O_4$ NPs/rGO composite could be a promising anode material for LIBs.

Table 1. Electrochemical performance of $ZnMn_2O_4$ electrode materials for LIBs.

Anode materials	Discharge capacity (mAh/g)	Cycle number	Current density (mA/g)	Ref.
$ZnMn_2O_4$@rGO-CNFs	1142	100	100	15
$ZnMn_2O_4$ hollow microspheres	750	120	400	17
Carbon-derivative-coated $ZnMn_2O_4$	700	500	500	20
$ZnMn_2O_4$/RGO	1082	90	100	32
$ZnMn_2O_4$@CMK-3 composites	997	100	100	44
Loaf-like $ZnMn_2O_4$ nanorods	517	100	500	45
$ZnMn_2O_4$ nanosheets	461	500	100	47
Nano-$ZnMn_2O_4$	716	90	100	48
$ZnMn_2O_4$/porous carbon framework	760	30	100	51
$ZnMn_2O_4$ NPs/rGO	1230	200	100	This work

To further elucidate the reasons for the different electrochemical performances between $ZnMn_2O_4$ NPs/rGO composites and pure $ZnMn_2O_4$ NPs, EIS measurements were carried out. As shown in Fig. 8(f), the EIS spectra consist of a semi-circle in the high to medium frequency region and an inclined line in the low frequency region. It is clearly seen from Fig. 8(f) that the half-circle diameter of $ZnMn_2O_4$ NPs/rGO electrode is smaller than that of $ZnMn_2O_4$ NPs electrode, indicating that $ZnMn_2O_4$ NPs/rGO composites have lower contact and charge-transfer resistance,[14] in good agreement with the higher conductivity of the $ZnMn_2O_4$ NPs/rGO composites.

To elucidate the electrochemical process more clearly, a detailed microstructure examination of the $ZnMn_2O_4$ NPs/rGO electrode (after 200 discharge cycles at 100 mA g^{-1}) was performed. As observed in Fig. 9(a), some crystalline materials are evidenced in the middle of the micrograph and the fringe spacing is measured to be 3.50 Å, which is consistent with the layered spacing of rGO.

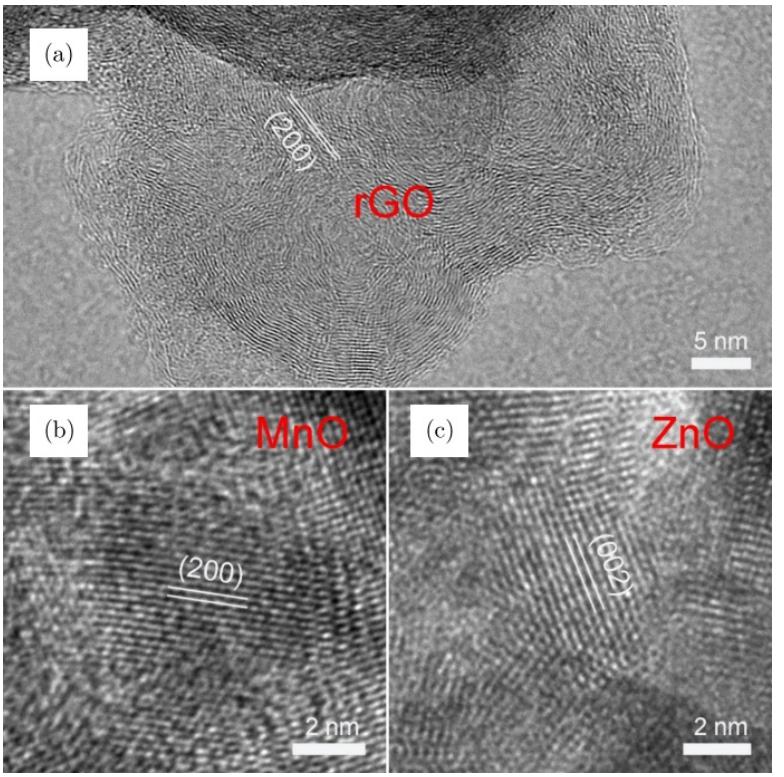

Fig. 9. Typical TEM image (a) and HRTEM images (b, c) of $ZnMn_2O_4$ NPs/rGO composite electrode after 200 cycles at a current density of 100 mA g^{-1}.

The interlayer spacing is slightly larger than the theoretical value of graphene, which is related to the intercalation of Li^+ in the graphene. It can be also seen from Fig. 9(a) that rGO displays a distinct amorphous feature with only a short-range order. The amorphous feature is transformed from an ordered structure due to the repeated Li^+ insertion/extraction in the electrochemical process. Figures 9(b) and 9(c) show typical HRTEM images of $ZnMn_2O_4$ NPs/rGO electrode after 200 cycles at 100 mA g^{-1}. The lattice spacing measured from Fig. 9(b) is 2.20 Å, which corresponds to the (200) planar spacing of MnO. The lattice spacing in Fig. 9(c) is measured to be 2.61 Å, which is consistent with the lattice spacing of (002) plane of ZnO. TEM results show that the $ZnMn_2O_4$ NPs decompose into ZnO NPs and MnO NPs after cycling, which is supported by CV curves shown in Fig. 8(a).

4. Conclusions

In summary, $ZnMn_2O_4$ NPs/rGO composites were fabricated through a two-step solvothermal method. The reversible capacity of composite electrode can reach 1230 mAh g^{-1} at a current density of 100 mAg^{-1} after 200 cycles. Owing to the introduction of rGO, the as-prepared $ZnMn_2O_4$ NPs/rGO composite electrode exhibits improved electrochemical performance. Compared to pure $ZnMn_2O_4$ NPs electrode, the $ZnMn_2O_4$ NPs/rGO composite electrode exhibits an improvement of approximately 47% with respect to capacity at a current density of 100 mAg^{-1} after 200 cycles. This mesoporous structure with a large specific area can provide excess active sites for storage of Li^+, and the introduction of rGO can enhance the conductivity of $ZnMn_2O_4$, which are favorable for rapid ion and electron transport during Li^+ insertion/extraction. This enhanced electrochemical performance is ascribed to the unique structure of compositing rGO with $ZnMn_2O_4$ NPs, which can promote the diffusion of Li^+, accelerate the electron transport and also buffer volume expansion during the electrochemical process. In addition, the rGO sheets can effectively prevent the agglomeration of $ZnMn_2O_4$ NPs, thus improving the electrochemical properties of the composite. The $ZnMn_2O_4$ NPs/rGO composite can be considered as a promising candidate for the anode materials of high-speed LIBs.

Acknowledgments

We thank the financial support from the National Natural Science Foundation of China (Grant Nos.: 10974105 and 21701095), the Natural Science Foundation of Shandong Province, China (Grant No.: ZR2017BEM007), China Postdoctoral Science Foundation (2017M622131), Program of Science and Technology for Higher Education in Shandong Province, China (Grant No.: J17KA010), Shandong Province "Double-Hundred Talent Plan" Program (Grant No.: WST2018006). Y. Q. Wang would also like to thank the financial support from the Taishan Scholar Program, and the Qingdao International Center for Semiconductor Photoelectric Nanomaterials and Shandong Provincial University Key Laboratory of Optoelectrical Material Physics and Devices. Meng Sun, Sijie Li and Jiajia Zou contributed to this work equally.

References

1. H. P. Yang, H. H. Wu, M. Y. Ge, L. J. Li, Y. F. Yuan, Q. Yao, J. Chen, L. F. Xia, J. M. Zheng, Z. Y. Chen, J. Duan, K. Kisslinger, X. C. Zeng, W. K. Lee, Q. B. Zhang and J. Lu, *Adv. Funct. Mater.* **29**, 1808825 (2019).
2. R. P. Fang, K. Chen, L. C. Yin, Z. H. Sun, F. Li and H. M. Cheng, *Adv. Mater.* **31**, 1800863 (2019).
3. M. Winter, B. Barnett and K. Xu, *Chem. Rev.* **118**, 11433 (2018).
4. Q. S. Wang, L. H. Jiang, Y. Yu and J. H. Sun, *Nano Energy* **55**, 93 (2019).
5. S. J. Ruan, A. Xiao, Z. F. Zheng, C. Ma, X. J. Liu, J. T. Wang, W. M. Qiao and L. C. Ling, *Nanoscale* **11**, 18290 (2019).
6. Y. H. Ding, B. Liu, J. J. Zou, H. Q. Liu, T. Xin, L. H. Xia and Y. Q. Wang, *Mater. Res. Bull.* **106**, 7 (2018).
7. H. Q. Liu, J. J. Zou, Y. H. Ding, B. Liu and Y. Q. Wang, *J. Appl. Electrochem.* **49**, 657 (2019).
8. J. W. Chen, X. Wang, J. X. Wang and P. S. Lee, *Adv. Energy Mater.* **6**, 1501745 (2016).
9. V. Aravindan, Y. S. Lee and S. Madhavi, *Adv. Energy Mater.* **5**, 1402225 (2015).
10. B. C. Sekhar, P. Packiyalakshmi and N. Kalaiselvi, *ChemElectroChem* **4**, 1154 (2017).
11. S. Q. Zhu, Y. Y. Shi, Q. L. Chen, Z. Y. Chen, R. Q. Bao, C. Yang, L. R. Hou, G. Pang and C. Z. Yuan, *RSC Adv.* **6**, 2024 (2016).
12. N. N. Wang, X. J. Ma, H. Y. Xu, L. Chen, J. Yue, F. E. Niu, J. Yang and Y. T. Qian, *Nano Energy* **6**, 193 (2014).

13. S. Chen, M. Y. Yao, F. Wang, J. G. Wang, Y. X. Zhang and Y. M. Wang, *Ceram. Int.* **45**, 5594 (2019).
14. D. P. Cai, D. D. Wang, H. Huang, X. C. Duan, B. Liu, L. L. Wang, Y. Liu, Q. H. Li and T. H. Wang, *J. Mater. Chem. A* **3**, 11430 (2015).
15. Q. L. Gao, Z. X. Yuan, L. X. Dong, G. F. Wang and X. B. Yu, *Electrochim. Acta* **270**, 417 (2018).
16. Y. Xiao, C. W. Hu and M. H. Cao, *J. Power Sources* **247**, 49 (2014).
17. G. Q. Zhang, L. Yu, H. B. Wu, H. E. Hoster and X. W. Lou, *Adv. Mater.* **24**, 4609 (2012).
18. L. F. Shen, Q. Che, H. S. Li and X. G. Zhang, *Adv. Funct. Mater.* **24**, 2630 (2014).
19. H. Li, T. B. Yang, B. Jin, M. Zhao, E. M. Jin, S. Jeong and Q. Jiang, *Inorg. Chem. Front.* **6**, 1535 (2019).
20. Z. J. Zhao, G. Y. Tian, A. Sarapulova, G. Melinte, J. L. Gomez-Urbano, C. P. Li, S. Y. Liu, E. Welter, M. Etter and S. Dsoke, *ACS Appl. Mater. Interfaces* **11**, 29888 (2019).
21. G. H. Qin, H. J. Zhang and C. Y. Wang, *J. Power Sources* **272**, 491 (2014).
22. J. L. Yang, J. J. Wang, D. N. Wang, X. F. Li, D. S. Geng, G. X. Liang, M. Gauthier, R. Y. Li and X. L. Sun, *J. Power Sources* **208**, 340 (2012).
23. K. P. Lopes, L. S. Cavalcante, A. Z. Simoes, J. A. Varela, E. Longo and E. R. Leite, *J. Alloys Compd.* **468**, 327 (2009).
24. S. Han, D. Q. Wu, S. Li, F. Zhang and X. L. Feng, *Small* **9**, 1173 (2013).
25. Q. Feng, Y. J. Du, S. Liang and H. B. Li, *Nanotechnology* **31**, 045402 (2019).
26. L. L. Chen, Z. H. Yang, H. G. Qin, X. Zeng, J. L. Meng and H. Z. Chen, *Electrochim. Acta* **317**, 155 (2019).
27. J. J. Zou, B. Liu, H. Q. Liu, Y. H. Ding, T. Xin and Y. Q. Wang, *Mater. Res. Bull.* **107**, 468 (2018).
28. X. W. Pan, Q. C. Du, Y. Zhou, L. C. Liu, G. Xu and C. Yan, *J. Nanosci. Nanotechnol.* **18**, 7231 (2018).
29. P. Xiong, B. R. Liu, V. Teran, Y. Zhao, L. L. Peng, X. Wang and G. H. Yu, *ACS Nano* **8**, 8610 (2014).
30. T. Zhang, H. J. Yue, H. L. Qiu, K. Zhu, L. J. Zhang, Y. J. Wei, F. Du, G. Chen and D. Zhang, *RSC Adv.* **5**, 99107 (2015).
31. Y. Luo, D. D. Yuan, M. S. Balogun, H. Yang, W. T. Qiu, J. C. Liu, P. Liu and Y. X. Tong, *J. Mater. Chem. A* **4**, 13431 (2016).
32. X. Liu, H. Xu, H. Ma, Z. Q. Tan, Y. D. Wang, Q. Z. Liu, M. F. Li, Y. L. Chen and D. Wang, *J. Alloys Compd.* **813**, 151598 (2020).
33. Z. G. Yin, J. W. Qin, W. Wang and M. H. Cao, *Nano Energy* **31**, 367 (2017).
34. P. J. Mafa, B. Ntsendwana, B. B. Mamba and A. T. Kuvarega, *J. Phys. Chem. C* **123**, 20605 (2019).
35. S. Ruan, A. Xiao, Z. Zheng, C. Ma, X. Liu, J. Wang, W. Qiao and L. Ling, *Nanoscale* **11**, 18290 (2019).
36. M. M. Sundaram, A. Biswal, D. Mitchell, R. Jones and C. Fernandez, *Phys. Chem. Chem. Phys.* **18**, 4711 (2016).
37. C. Z. Yuan, L. H. Zhang, L. R. Hou, L. Zhou, G. Pang and L. Lian, *Chem. -Eur. J.* **21**, 1262 (2015).
38. S. W. Kim, H. W. Lee, P. Muralidharan, D. H. Seo, W. S. Yoon, D. K. Kim and K. Kang, *Nano Res.* **4**, 505 (2011).
39. S. H. Li, J. W. Chen, M. Q. Cui, G. F. Cai, J. X. Wang, P. Cui, X. F. Gong and P. S. Lee, *Small* **13**, 1602893 (2017).
40. L. P. Yang, J. H. Kong, W. A. Yee, W. S. Liu, S. L. Phua, C. L. Toh, S. Huang and X. H. Lu, *Nanoscale* **4**, 4968 (2012).
41. Y. J. Sun, Z. W. Zhao, F. Dong and W. Zhang, *Phys. Chem. Chem. Phys.* **17**, 10383 (2015).
42. V. Etacheri, G. A. Seisenbaeva, J. Caruthers, G. Daniel, J. M. Nedelec, V. G. Kessler and V. G. Pol, *Adv. Energy Mater.* **5**, 1401289 (2015).
43. T. Zhang, H. L. Qiu, M. Zhang, Z. B. Fang, X. S. Zhao, L. Wang, G. Chen, Y. J. Wei, H. J. Yue, C. Z. Wang and D. Zhang, *Carbon* **123**, 717 (2017).
44. Z. C. Bai, N. Fan, C. H. Sun, Z. C. Ju, C. L. Guo, J. Yang and Y. T. Qian, *Nanoscale* **5**, 2442 (2013).
45. L. L. Peng, P. Xiong, L. Ma, Y. F. Yuan, Y. Zhu, D. H. Chen, X. Y. Luo, J. Lu, K. Amine and G. H. Yu, *Nat. Commun.* **8**, 15139 (2017).
46. S. Z. Gu, J. Xu and B. A. Lu, *Energy Technol.* **4**, 1106 (2016).
47. T. Zhang, Y. Gao, H. J. Yue, H. L. Qiu, Z. D. Guo, Y. J. Wei, C. Z. Wang, G. Chen and D. Zhang, *Electrochim. Acta* **198**, 84 (2016).
48. X. Y. Zhao, M. H. Cao, B. Liu, Y. Tian and C. W. Hu, *J. Mater. Chem.* **22**, 13334 (2012).
49. S. L. Gu and A. P. Zhu, *J. Alloys Compd.* **813**, 152160 (2020).
50. P. Li, J. Y. Liu, Y. Liu, Y. W. Wang, Z. T. Li, W. T. Wu, Y. Wang, L. H. Yin, H. Xie, M. B. Wu, X. J. He and J. S. Qiu, *Electrochim. Acta* **180**, 164 (2015).
51. Z. Y. Wang and C. J. Liu, *Nano Energy* **11**, 277 (2015).
52. L. Pan, X. D. Zhu, X. M. Xie and Y. T. Liu, *Adv. Funct. Mater.* **25**, 3341 (2015).